IEEE *Access*

Research and Experiment of Repairable Space Telescope Interface System

ZHEN SHI [ID]1,2, WEIGUO ZHAO1, LIBAO YANG1, YANG XUN1, QINGYA LI1, AND YAOYU ZHANG1

[1]Changchun Institute of Optics, Fine Mechanics and Physics, Chinese Academy of Sciences, Changchun 130033, China
[2]University of Chinese Academy of Sciences, Beijing 100049, China

Corresponding author: Libao Yang (yanglibao228@163.com)

ABSTRACT Space technology is the core competitiveness of a powerful country. Space maintenance technology has just started in our country. The biggest innovation of this article is to design a set of interface system, which is suitable for on-orbit maintenance of space science instruments. It represents that this technology from scratch in our country. A new measuring method is proposed. According to the homogeneous coordinate transformation, the mathematical models of the relationships between fit clearances of interface system and the six-degree of freedom change of the maintenance module are derived. According to the index requirements, the corresponding fit clearance and repeat positioning accuracy are determined. Set up an experimental platform, and use autocollimator and laser tracker to measure the repeated positioning accuracy of the module. Based on the theory of small displacement, the least square method is used to deduce the rotation angle and translation amount of the module through the change of the characteristic point coordinates. The experiment proves that the interface meets the requirement of on-orbit maintainable operation, and the experimental data proves that the theoretical equation is correct. Providing engineering reference for other space maintenance scientific instruments.

INDEX TERMS On-orbit maintenance, interface system, repeat positioning accuracy, fit clearance.

I. INTRODUCTION

In a complex space environment, all space science instruments may at any time affect their value due to failure, degradation or obsolescence. And most of the spacecraft on-orbit fault is usually only a problem with individual component. These problems will cause the space science instrument function decline, or even lead to the loss of the entire spacecraft function, forming a huge waste. Re-launching spacecraft to replace them would only lead to increased costs, but space maintenance and service technologies could effectively address this problem. On-orbit maintenance can quickly restore its functions, which has good timeliness and economy. Secondly, the reliability of the whole machine can be effectively improved by replacing the vulnerable and consumable parts [1].

NASA astronauts repaired the skylab solar windsurfing board on May 26, 1975, which was the first repair operation carried out by mankind in space [2]. The on-orbit capture of

The associate editor coordinating the review of this manuscript and approving it for publication was Jingang Jiang [ID].

the SMM probe in April 1984 was the first time in human history to repair a satellite in space orbit [3]. The MIR space station launched by the Soviet Union in 1986 was the first modular space station assembled on-orbit in human history [4]. Typical on-orbit maintenance tasks include Japan's ETS-VII(Engineering Test Satellite-VII); America's Orbital Express; German Robot Technology Experiment [5]–[7]. And the most representative one is the HST launched in 1990. During the more than ten years from 1993 to 2009, the Hubble Telescope accepted five on-orbit service tasks. Including repairs, replacement of faulty parts, equipment upgrades and installation of new measuring elements. Hubble's detection capability has been increased by 70 times and its life span has been extended through on-orbit maintenance, contributing endless power to scientific research [8]–[12].

Before and after the replacement of the back-end module of the space telescope, the stability of the optical focal plane directly determines the imaging quality, and the stability of the focal plane is closely related to the spatial layout of the back-end module interface. Chen Xiqu studied

the effect of substrate temperature on the focal plane array [13]; Zhang Yong studied the adjustable focal length and controllable focal plane of a liquid crystal lens driven by a double electrode [14]; Li Jin studied the focal plane of the collimator for geometric calibration of optical cameras [15]. The clearance of the interface mechanism determines the repeated positioning accuracy of the back-end module, which must be reasonably allocated. A large number of scholars have studied the clearance: Ravindra Arora studied the influence of electrical clearance in air for overhead traction system [16]; Xu Minmin studied the influence of rolling bearing radial clearance on the state of wind turbine [17]; Gu Yingkui studied the effect of bearing clearance on dynamic characteristics of a spur gear system [18]; Teng Fei studied the effect of variation mechanism of three-dimensional blade tip clearance on aero-engine [19].

This article takes the on-orbit maintenance of the space telescope as the research object, and a set of interface mechanism is designed in detail to meet the requirements of on orbit thermal stress release according to the kinematics principle. According to the homogeneous coordinate transformation, the theoretical equations of rotation angle and fit clearance are deduced, and the best fit clearance satisfying the repeated positioning accuracy is given. The space microgravity environment is simulated, and the measured rotation angle and translation by the autocollimator and laser tracker. The experimental data shows that the theoretical equation is correct, the clearance is reasonable, and the index requirements are met.

The paper is organized as follows: Section 2 introduces the positioning principle and spatial layout of the interface system. According to the principle of focal plane stability, the best spatial distribution of the interface is given. Section 3 introduces the mathematical model of repeated positioning accuracy and distributes the interface clearance reasonably according to the requirement of the index. Section 4 introduces the internal composition and detailed design of the interface system. Section 5 introduces the experimental method of repeatable positioning accuracy of the back-end module and analyzes the experimental data. Section 6 draws conclusion.

II. POSITIONING PRINCIPLE AND SPATIAL LAYOUT OF INTERFACE

A. POSITIONING PRINCIPLE OF INTERFACE

The two mechanical modules that need to be connected to the maintainable interface have separable ability. The separated two mechanical modules have good reset ability through the connectable interface and can maintain good position stability. The interface structure cannot have problems such as over-constrained or under-constrained. After the space telescope is put into orbit, the deformation between the optical system and the supporting structure is greater than the allowable deformation of the optical system due to gravity unloading, stress release, thermal deformation and other factors. In order to ensure the stability of the focal plane, a method

must be adopted to isolate the optical system to avoid the influence of unknown stress. The idea of kinematic connection comes from multi-degree-of-freedom robot, which can release the thermal stress well and maintain high stiffness and pointing accuracy by removing the degree of freedom constraint of deformation direction. The calculation equation of spatial degree of freedom is (1).

$$f = 6(n - j - 1) + \sum_{i=1}^{j} p_i \qquad (1)$$

In (1), f is the degree of freedom of mechanism, n is the number of components, j is the number of kinematic pairs, p_i is the degree of freedom of the i kinematic pair. As shown in Fig. 1, the interface mechanism adopts three points support. Interface A restricts the three translation of the module in space and releases three rotational degrees of freedom in space. Interface B restricts the translation of the module along the Y and Z directions, releasing the other four degrees of freedom. Support point A and B together restrict the rotation of the module around the X and Z directions. Interface C restricts the translation of the module along the Z direction and releases the other 5 degrees of freedom. The three points ABC together restrict the rotation of the module around the Y direction. In this system, the components include optical instrument and installation platform. The number of components is 2 and the number of kinematic pairs is 3, that is, n is 2 and j is 3. The degrees of freedom of each kinematic pair are 3, 4 and 5 respectively. And (1) is used to solve for f as 0. The three support points of ABC jointly realize the statically determinate support of the module [20].
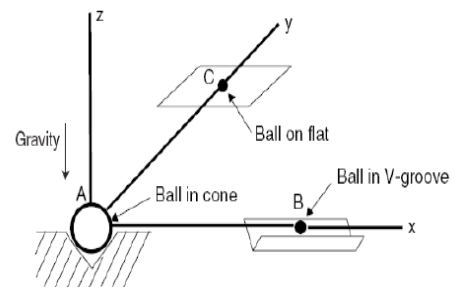

FIGURE 1. Schematic diagram of kinematic positioning.

The principle of releasing thermal stress on-orbit: Since the degrees of freedom of the three translation directions of point A are completely limited, when the space temperature changes, the module will deform uniformly along the XY directions. Point B moves along the axial direction and point C moves on the XY plane. The entire module will only produce rotational deformation around point A on the XY plane. The thermal stress and thermal deformation caused by the temperature are released through the translational movement of the module. The interface structure is designed using kinematics principles, which is suitable for installation of space science instruments with drastic temperature

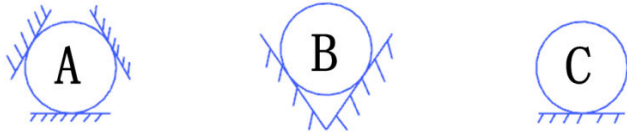changes, ensuring the long-term normal operation of the whole machine on-orbit.

FIGURE 2. Contact diagram of kinematics principle three-point positioning ball.

B. SPACE LAYOUT OF INSTALLATION INTERFACE

The plane of three points ABC is parallel to the focal plane, and the center of the three points coincides with the projection of the center of the focal plane in the direction of the optical axis. Point C is located at the front of the module, two points AB are located on either side of the module. The projection of the three points ABC on the XY plane is shown in Fig. 3-a. The amount of change in the center of the triangle represents the pointing accuracy of the entire focal plane. The interface mechanism and the back-end module form a square with side length L. When the temperature changes, the changes of three points ABC are shown in Fig. 3-b.
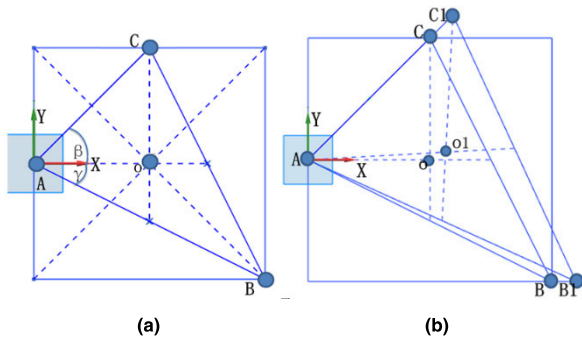

FIGURE 3. The projection of three points ABC in the XY plane. (a) Position before temperature change. (b) Position after temperature change.

As shown in the Fig. 3, the coordinate system is established with the origin of point A, the Z axis is perpendicular to the paper and outward. Only knows that AB is located on both sides of the module and C is located inside the module. Table 1 below is the spatial coordinates of the three points ABC.

TABLE 1. Spatial Coordinates of the Three Points ABC.

	X	Y	Z
A	0	0	0
B	L	B_Y	0
C	C_X	C_Y	0

Among them, the unknown variable is B_Y, C_X, C_Y, their variation is $0 - L$. The center of the triangle formed by ABC three points should coincide with the center of the square

whose side length is L. Therefore, we have the following (2).

$$\begin{cases} C_X = \dfrac{L}{2} \\ 2C_Y - B_Y = \dfrac{3L}{2} \end{cases} \tag{2}$$

When the temperature change is ΔT, The coefficient of thermal expansion of the module is a. The variation of point B in X direction and the variation of point B in XY directions are (3).

$$\begin{cases} \Delta BB1_X = a\Delta TL_{AB} \cos\gamma \\ \Delta CC1_X = a\Delta TL_{AC} \cos\beta \\ \Delta CC1_Y = a\Delta TL_{AC} \sin\beta \end{cases} \tag{3}$$

In the Fig. 3, O is the centroid of the triangle formed by three points, $O1$ is the centroid of the three points after the temperature change, where the change of the centroid is the pointing accuracy of the focal plane of the back-end module, which is (4).

$$\begin{cases} \Delta OO1_X = \dfrac{\Delta BB1_X + \Delta CC1_X}{3} \\ \Delta OO1_Y = \dfrac{\Delta CC1_Y}{3} \end{cases} \tag{4}$$

In order to obtain the highest pointing accuracy under the same temperature change, (4) is the smallest, we obtain: $B_Y = -\frac{L}{2}, C_Y = \frac{L}{2}$

III. THEORETICAL CALCULATION OF REPEATED POSITIONING ACCURACY

A. POSE TRANSFORMATION MATRIX

The translation and rotation angle of the back-end module after the replacement are $(T_X, T_Y, T_Z, R_X, R_Y, R_Z)$. The rigid body fixed coordinate system and the reference coordinate system coincide before the change. It is assumed that the position change sequence of the rigid body is rotated around the X-axis, Y-axis, and Z-axis of the reference coordinate system in turn, and finally it is translated along the three axes. The fixed coordinate system of the rigid body becomes blue after rotating around the X-axis, becomes green after rotating around the Y-axis, and becomes pink after rotating around the Z-axis. The color of the fixed coordinate system is still pink after the translation change. The change process is shown in Fig. 4.
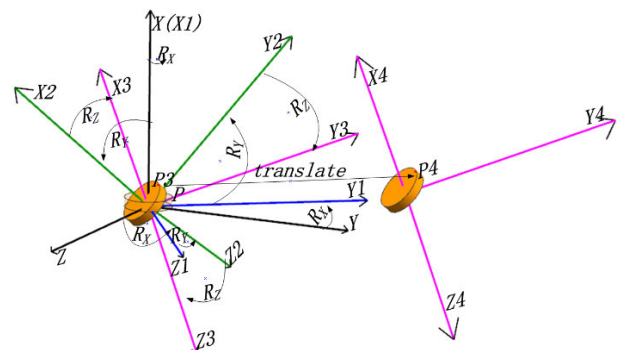

FIGURE 4. Spatial change process of rigid body.

The point P on the rigid body becomes $P3$ after three rotation transformations and then P4 after translation. The change from point P to $P4$ is realized through the change matrix F.

$$T = \begin{bmatrix} 1 & 0 & 0 & T_X \\ 0 & 1 & 0 & T_Y \\ 0 & 0 & 1 & T_Z \\ 0 & 0 & 0 & 1 \end{bmatrix}$$

$$Rot_Z = \begin{bmatrix} \cos R_Z & -\sin R_Z & 0 & 0 \\ \sin R_Z & \cos R_Z & 0 & 0 \\ 0 & 0 & 1 & 0 \\ 0 & 0 & 0 & 1 \end{bmatrix}$$

$$Rot_Y = \begin{bmatrix} \cos R_Y & 0 & \sin R_Y & 0 \\ 0 & 1 & 0 & 0 \\ -\sin R_Y & 0 & \cos R_Y & 0 \\ 0 & 0 & 0 & 1 \end{bmatrix}$$

$$Rot_X = \begin{bmatrix} 1 & 0 & 0 & 0 \\ 0 & \cos R_X & -\sin R_X & 0 \\ 0 & \sin R_X & \cos R_X & 0 \\ 0 & 0 & 0 & 1 \end{bmatrix} \quad (5)$$

$$F = TRot_Z Rot_Y Rot_X \quad (6)$$

Solve the (6), as shown at the bottom of the page.

When the rotation angle of the rigid body around the three axes are less than 30", (6) can be simplified as (7).

$$F_1$$
$$= \begin{bmatrix} 1 & -R_Z & R_Y & T_X \\ R_Z & 1 & -R_X & T_Y \\ -R_Y & R_X & 1 & T_Z \\ 0 & 0 & 0 & 1 \end{bmatrix} \quad (7)$$

$$MAX\nabla F$$
$$= F - F_1$$
$$= \begin{bmatrix} \pm 2.11 \times 10^{-8} & \pm 2.12 \times 10^{-8} & \pm 2.12 \times 10^{-8} & 0 \\ \pm 2.05 \times 10^{-12} & \pm 2.12 \times 10^{-8} & \pm 2.11 \times 10^{-8} & 0 \\ \pm 5.13 \times 10^{-13} & \pm 2.05 \times 10^{-12} & \pm 2.11 \times 10^{-8} & 0 \\ 0 & 0 & 0 & 1 \end{bmatrix}$$
$$\quad (8)$$

At this time, the magnitude of the maximum difference between (6) and (7) is 10^{-8}, which can be considered negligible. Proving $F = F_1$. Therefore, the position transformation matrix of the rigid body is expressed as F_1. Similarly, when the rotation angle of the module around each axis is less than 30", the rotation order or translation order around XYZ axes can be changed at will. There are 24 different combinations of the form of the module change matrix F, all of which can be approximated with F_1 Means.

B. ANGLE ERROR ANALYSIS

According to formula F_1, we believe that the theoretical rotation angle of the rigid body are R_X, R_Y, R_Z, but the real rotation angle of the rigid body after spatial change is expressed as R_{X1}, R_{Y1}, R_{Z1}. The real rotation angle of the rigid body around each axis can be expressed as the spatial coordinate change of the other axis unit vectors. i, j, k are the unit vector of the three axes in the reference coordinate system, and (9) represents i, j, k.

$$\begin{bmatrix} i & j & k \end{bmatrix} = \begin{bmatrix} 1 & 0 & 0 \\ 0 & 1 & 0 \\ 0 & 0 & 1 \end{bmatrix} \quad (9)$$

The three unit vectors change to i', j', k' after spatial variation in (10), as shown at the bottom of the page.

The direction of space vector remains unchanged after translation. In order to simplify the calculation, the translation of the rigid body is omitted. After the rigid body changes, the real rotation angle of X-direction can be expressed as the angle between j'_{YZ} of the projection of j' onto the YZ plane and j, or, the angle between k'_{YZ} of the projection of k' onto the YZ plane and k. The real rotation angle of Y-direction can be expressed as the angle between i'_{XZ} of the projection of i' onto the XZ plane and i, or, the angle between k'_{XZ} of the projection of k' onto the XZ plane and k. The real rotation angle of Z-direction can be expressed as the angle between i'_{XY} of the projection of i' onto the XY plane and i, or, the angle between j'_{XY} of the projection of j' onto the XY plane and j.

$$F = \begin{bmatrix} \cos R_Y \cos R_Z & \cos R_Z \sin R_Y \sin R_X - \sin R_Z \cos R_X & \cos R_Z \sin R_Y \cos R_X + \sin R_Z \sin R_X & T_X \\ \sin R_Z \cos R_Y & \sin R_Z \sin R_Y \sin R_X + \cos R_Z \cos R_X & \sin R_Z \sin R_Y \cos R_X - \sin R_X \cos R_Z & T_Y \\ -\sin R_Y & \sin R_X \cos R_Y & \cos R_X \cos R_Y & T_Z \\ 0 & 0 & 0 & 1 \end{bmatrix}$$

$$\begin{bmatrix} i' & j' & k' \\ 1 & 1 & 1 \end{bmatrix}$$
$$= F_1 \begin{bmatrix} i & j & k \\ 1 & 1 & 1 \end{bmatrix}$$
$$\begin{bmatrix} \cos R_Y \cos R_Z + T_X & \cos R_Z \sin R_Y \sin R_X - \sin R_Z \cos R_X + T_X & \cos R_Z \sin R_Y \cos R_X - \sin R_Z \sin R_X + T_X \\ \sin R_Z \cos R_Y + T_Y & \sin R_Z \sin R_Y \sin R_X - \cos R_Z \cos R_X + T_Y & \sin R_Z \sin R_Y \cos R_X - \sin R_X \cos R_Z + T_Y \\ \sin R_Y + T_Z & \sin R_X \cos R_Y + T_Z & \cos R_X \cos R_Y + T_Z \end{bmatrix}$$
$$\quad (10)$$

When j is used to represent R_{X1} in (11), as shown at the bottom of the page.

When the rotation angles of rigid body around three axes are close to zero, the above (11) can be simplified as

$$R_{X1} = arccos < j'_{YZ}, j >= \frac{\cos R_Z \cos R_X}{\sqrt{(\sin R_X)^2 + (\cos R_Z \cos R_X)^2}} \tag{12}$$

When k is used to represent R_{X1} in (13), as shown at the bottom of the page.

When the rotation angles of rigid body around three axes are close to zero, the above (13) can be simplified as

$$R_{X1} = arccos < k'_{YZ}, k >= \frac{\cos R_X \cos R_Y}{\sqrt{(\cos R_X \cos R_Y)^2 + (\sin R_X)^2}} \tag{14}$$

When the rotation angles of rigid body around three axes are close to zero, (12) and (14) have the same expression. Therefore, the value of the rotation angle in the X-direction is unique.

$$\frac{R_{X1}}{R_X} = \frac{arccos < j'_{YZ}, j >}{R_X} \approx \frac{arccos < k'_{YZ}, k >}{R_X} \approx 1 \tag{15}$$

When k is used to represent R_{Y1}

$$R_{Y1} = arccos < i'_{XZ}, i >= \frac{\cos R_Y \cos R_Z}{\sqrt{(\cos R_Y \cos R_Z)^2 + (\sin R_Y)^2}} \tag{16}$$

When k is used to represent R_{Y1} in (17), as shown at the bottom of the page.

When the rotation angles of rigid body around three axes are close to zero, the above (17) can be simplified as

$$R_{Y1} = arccos < k'_{XZ}, k >= \frac{\cos R_Y \cos R_X}{\sqrt{(\cos R_Y \cos R_X)^2 + (\sin R_Y)^2}} \tag{18}$$

When the rotation angles of rigid body around three axes are close to zero, (16) and (18) have the same expression. Therefore, the value of the rotation angle in the Y- direction is unique.

$$\frac{R_{Y1}}{R_Y} = \frac{arccos < i'_{YZ}, i >}{R_Y} \approx \frac{arccos < k'_{YZ}, k >}{R_Y} \approx 1 \tag{19}$$

When i is used to represent R_{Z1}

$$R_{Z1} = arccos < i'_{XY}, i >$$
$$= \frac{\cos R_Y \cos R_Z}{\sqrt{(\cos R_Y \cos R_Z)^2 + (\sin R_Z \cos R_Y)^2}} \tag{20}$$

When the rotation angles of rigid body around three axes are close to zero, the above (20) can be simplified as

$$R_{Z1} = arccos < i'_{XY}, i >= \frac{\cos R_Y \cos R_Z}{\sqrt{(\cos R_Y \cos R_Z)^2 + (\sin R_Z)^2}} \tag{21}$$

When j is used to represent R_{Z1} in (22), as shown at the bottom of the page.

When the rotation angles of rigid body around three axes are close to zero, the above (22) can be simplified as

$$R_{Z1} = arccos < j'_{XY}, j >= \frac{\cos R_Z \cos R_X}{\sqrt{(\cos R_Z \cos R_X)^2 + (\sin R_Z)^2}} \tag{23}$$

When the rotation angles of rigid body around three axes are close to zero, (21) and (23) have the same expression. Therefore, the value of the rotation angle in the Z- direction is unique.

$$\frac{R_{Z1}}{R_Z} = \frac{arccos < i'_{XY}, i >}{R_Z} \approx \frac{arccos < j'_{XY}, j >}{R_Z} \approx 1 \tag{24}$$

When the rotation angles of rigid body around three axes are close to zero, the rotation angle of a rigid body around each axis has the same form. Taking the X-direction as a reference, the difference between the real and theoretical rotation angles is expressed as ΔR_X.

$$\Delta R_X = |R_{X1}| - |R_X| \tag{25}$$

We can see from (12) and (13) that there are only two variables, so ΔR_X can be simplified to a function with only two variables. Suppose that two different variables have the same variation range, draw the following Fig. 5. When the rotation angle of the rigid body around each axis is less than30'', it can be seen that the maximum value of ΔR_X is 0.00003''. Similarly, the rotation angle around YZ axis has the same conclusion. Therefore, the theoretical rotation angle of

$$R_{X1} = arccos < j'_{YZ}, j >= \frac{\sin R_Z \sin R_Y \sin R_X + \cos R_Z \cos R_X}{\sqrt{(\sin R_X \cos R_Y)^2 + (\sin R_Z \sin R_Y \sin R_X + \cos R_Z \cos R_X)^2}} \tag{11}$$

$$R_{X1} = arccos < k'_{YZ}, k >= \frac{\cos R_Y \cos R_X}{\sqrt{(\cos R_Y \cos R_X)^2 + (\sin R_Z \sin R_Y \cos R_X - \sin R_X \cos R_Z)^2}} \tag{13}$$

$$R_{Y1} = arccos < k'_{XZ}, k >= \frac{\cos R_Y \cos R_X}{\sqrt{(\cos R_Y \cos R_X)^2 + (\cos R_Z \sin R_Y \cos R_X + \sin R_X \sin R_Z)^2}} \tag{17}$$

$$R_{Z1} = arccos < j'_{XY}, j >= \frac{\sin R_Z \sin R_Y \sin R_X + \cos R_Z \cos R_X}{\sqrt{(\sin R_Z \sin R_Y \sin R_X + \cos R_Z \cos R_X)^2 + (\cos R_Z \sin R_Y \sin R_X - \sin R_Z \cos R_X)^2}} \tag{22}$$
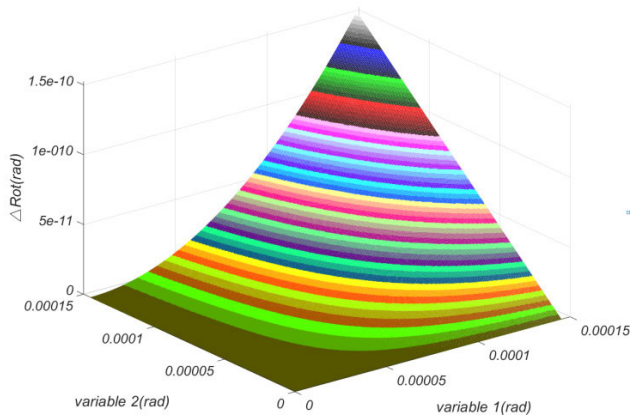
FIGURE 5. The relationship between the difference between the theoretical rotation angle and the real rotation angle of a rigid body with two variables.

rigid body can nearly equal to the real rotation angle of rigid body.

Similarly, when the rotation angle of the module around each axis is less than 30'', the rotation order or translation order around *XYZ* axes can be changed at will. The theoretical rotation angle of rigid body can replace the real rotation angle of rigid body.

C. THEORETICAL REPEATED POSITIONING ACCURACY ANALYSIS

The spatial coordinates of each feature point on the rigid body in reference coordinate system are X_i, Y_i, Z_i. After the change, the spatial coordinates of the feature point in the reference coordinate system are (X_i', Y_i', Z_i').

According to the homogeneous coordinate transformation, (26) can be obtained.

$$\begin{cases} X_i' = X_i - Y_iR_Z + Z_iR_Y + T_X \\ Y_i' = X_iR_Z + Y_i - Z_iR_X + T_Y \\ Z_i' = -X_iR_Y + Y_iR_X + Z_i + T_Z \end{cases} \quad (26)$$

The coordinate variation of the characteristic points on the rigid body is (d_{Xi}, d_{Yi}, d_{Zi}).

$$(d_{Xi}, d_{Yi}, d_{Zi}) = (X_i', Y_i', Z_i') - (X_i, Y_i, Z_i)$$

$$\begin{cases} d_{Xi} = -Y_iR_Z + Z_iR_Y + T_X \\ d_{Yi} = X_iR_Z - Z_iR_X + T_Y \\ d_{Zi} = -X_iR_Y + Y_iR_X + T_Z \end{cases} \quad (27)$$

The translation and angle change of the plane formed by the three points *ABC* is used as the pose change of the entire back-end module. The clearance between the three points *ABC* determines the limit value of the three-point change. Among them, point *A* restricts the degree of freedom of translation in the *XYZ* directions, point *B* restricts the degree of freedom of translation in the *YZ* direction, and point *C* restricts the degree of freedom of translation in the *Z* direction; Combined with Fig. 2, it can be obtained (29). Suppose the fit clearance of three points *ABC* is $(\nabla t_A, \nabla t_B, \nabla t_C)$.

According to the requirements of the index, the maximum rotation angle of the module is less than 20 ''. Put the spatial coordinates of the three points *A* (0, 0, 0) *B* (500, -250, 0) *C* (250, 250, 0) into the following (28) -(29).

$$\begin{bmatrix} 1 & 0 & 0 & 0 & z_A & -y_A \\ 1 & 0 & 0 & 0 & z_B & -y_B \\ 1 & 0 & 0 & 0 & z_C & -y_C \\ 0 & 1 & 0 & -z_A & 0 & x_A \\ 0 & 1 & 0 & -z_B & 0 & x_B \\ 0 & 1 & 0 & -z_C & 0 & x_C \\ 0 & 0 & 1 & y_A & -x_A & 0 \\ 0 & 0 & 1 & y_B & -x_B & 0 \\ 0 & 0 & 1 & y_C & -x_C & 0 \end{bmatrix} \begin{bmatrix} T_x \\ T_y \\ T_z \\ R_x \\ R_y \\ R_z \end{bmatrix} = \begin{bmatrix} d_{x_A} \\ d_{x_B} \\ d_{x_c} \\ d_{y_A} \\ d_{y_B} \\ d_{y_c} \\ d_{z_A} \\ d_{z_B} \\ d_{z_c} \end{bmatrix} \quad (28)$$

$$\begin{cases} (d_{XA})^2 + (d_{YA})^2 + (d_{ZA})^2 \leq \left(\dfrac{\nabla t_A}{2}\right)^2 \\ (d_{YB})^2 + (d_{ZB})^2 \leq \left(\dfrac{\nabla t_B}{2}\right)^2 \\ (d_{ZC})^2 \leq \left(\dfrac{\nabla t_B}{2}\right)^2 \end{cases} \quad (29)$$

Solved: $\nabla t_A = 0.02424mm$, $\nabla t_B = 0.07272mm$, $\nabla t_C = 0.02424mm$ Finally, the fitting tolerance of each point is selected, and the clearance value of point *A* and point *C* is 0.02*mm*, the clearance value of point *B* is 0.05*mm*. Solution (28), As can be seen from Fig. 6:

$$\max R_X = \pm 15.1'', \max R_Y = \pm 15.1'', \max R_z = \pm 14.4''$$

$$\max T_X = \max T_Y = \max T_Y = \pm 0.01mm$$

IV. INTERFACE SYSTEM DESIGN

The *A*-point mechanism adopts a typical ball head-ball socket structure, which is characterized by limiting the three-dimensional translational freedom of the ball in the socket and releasing the rotational freedom in all directions. And integrate the electric drive locking mechanism to form the *A*-point positioning locking point, where the locking is to deal with the huge impact of the rocket when it is launched. It is released automatically by the electric drive after on-orbit. *A*-Point mechanism consists of positioning ball, ball and socket assembly, operating rod, locking mechanism, L plate, etc. The specific model is shown in Fig. 7-a: The connection between the L plate and the module are called the moving part, the connection between the ball-socket assembly and the module frame are called the fixed part. As shown in Fig. 7-a, the connection of *A*-point can be tightened and separated by the rotation of the screw thread. The ball-socket assembly is composed of the ball-socket base and the ball. Meanwhile, the ball can only rotate freely in the socket and cannot be detached. In order to enable the screw to be accurately imported into the ball socket, a polished rod is set between the ball head and the thread at the front end of the screw for easy import. When the two parts of the ball head and the ball socket are firmly connected, the ball can be closely attached to the ball socket by the screw to form a closed ball head-ball socket structure. In this way, the three-dimensional
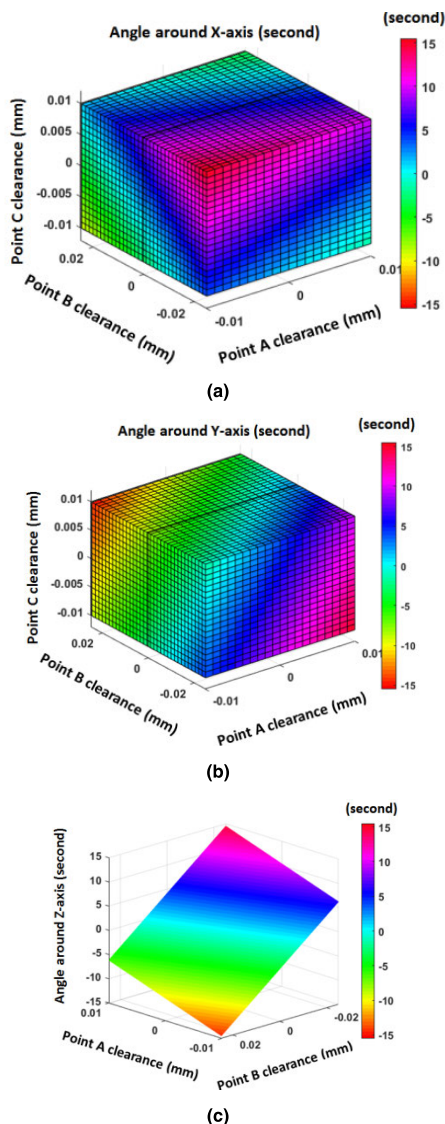
FIGURE 6. The rotation angle range of the module under a given clearance. (a) Rotation angle range around X-axis; (b) Rotation angle range around Y-axis ;(c) Rotation angle range around Z-axis.

FIGURE 7. Three point interface structure diagram. (a) Interface structure of A-point; (b) Interface structure of B-point; (c) Interface structure of C-point.

translational freedom of the ball in the sphere nest is limited and the freedom of rotation in each direction is released.

The B-point mechanism is a typical shaft-hole structure, which can realize the restriction of two-dimensional translational freedom and releases the translation of the other dimension and three-dimensional rotational freedom. The shaft is inserted and pulled out with a rack and pinion structure to realize the lateral movement of the shaft, and finally realize the lateral positioning function when the module is fixed. The B-point mechanism consists of positioning shaft sleeve, positioning shaft, positioning hole seat, eliminate gap component, locking mechanism, operating rod, etc. As shown in Fig. 7-b: The connection between the positioning shaft sleeve and the module are called a moving block, and the connection between the positioning hole seat and the module frame are called a fixed block. Under the condition of gravity
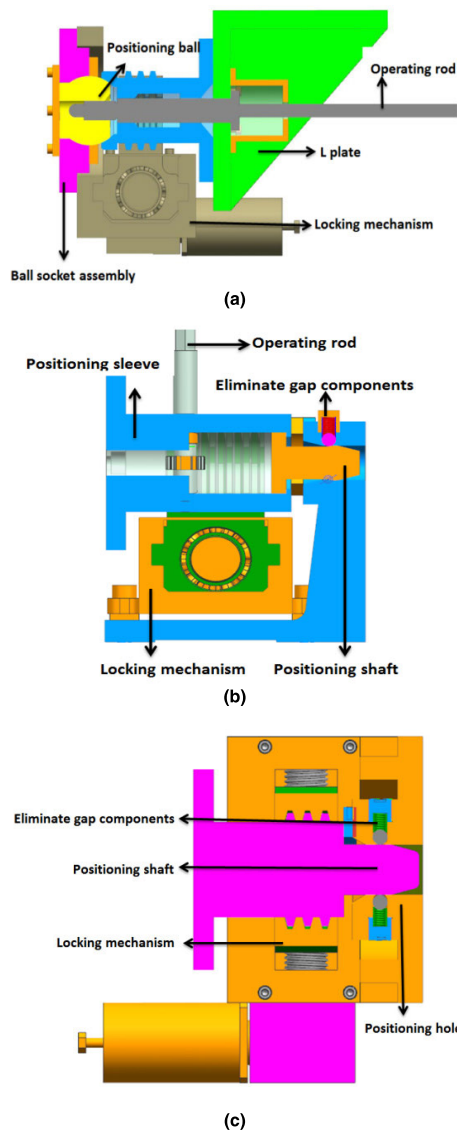
installation, B-point combined with A-point play the role of carrying the force of gravity, and the linking process needs to overcome gravity. The positioning stage requires position stability, so there is an eliminate gap component at the front of B-point. The ball head and the positioning hole are fitted with clearance to facilitate the shaft insertion and extraction. The clearance elimination and positioning function is realized by using elastic steel ball components. The three groups of elastic steel ball components are distributed in a circumferential symmetry to balance the application of force. And the elastic steel ball component is stuck at the position $1.5mm$ of the front end of the positioning ball head, which play the role of elastic pre-tensioning and preventing loosening.

The C-point mechanism adopts a typical key-slot structure, which is used to limit the degree of freedom in one direction. It also integrates an electric drive locking mechanism.

The *C*-point mechanism is composed of positioning shaft, positioning hole, eliminate gap components, locking mechanism, etc. As shown in Fig. 7-c: The ball head and the positioning hole are fitted with clearance to facilitate the shaft insertion and extraction. In addition, the clearance elimination and positioning function is realized by elastic steel ball assembly. The two sets of elastic steel ball components are distributed symmetrically, acting as a balanced force. The elastic steel ball is pre-tensioned by a compression spring with an elastic coefficient of $11N/mm$. When the spring is compressed, two sets of pre-tension forces will axially restrain the positioning shaft.

V. EXPERIMENTAL VERIFICATION
A. THE EXPERIMENTAL PRINCIPLE

The plane formed by the three points *ABC* should be parallel to the direction of disassembly and assembly of the module. Point *C* is located at the front end of the module, and the first contact is achieved when the module is pushed to the positioning position. The positioning shaft installed on the module is the ball head, and the corresponding rectangular hole on the module frame. The axis of the positioning shaft is consistent with the direction of disassembly and assembly. Therefore, the positioning and disengagement of point *C* is directly realized by disassembling the module without additional operations. This is the main difference from points *A* and *B*. Point *A* is located on the side of the module, and cooperate after contact at point *C*. On the module is a ball and socket structure, and on the module frame is a combination of a positioning ball with a screw hole and a ball- socket seat. The two work together to make the module as a whole tighten. Point *B* is located on the other side of the module, the locating shaft of the ball head is installed on the module, and the circular hole is installed on the module frame. Since the axis of the *B*-point positioning shaft is perpendicular to the installation direction, the positioning shaft of *B*-point on the module is last pushed into the corresponding positioning hole. And at the same time, when the module exits, the positioning shaft of *B*-point must first exit along the axis direction.

The micro-gravity simulation ground test includes the falling tower method, which is implemented by building high towers on the ground or digging deep wells; Weightless airplane method, the plane flies in a parabolic attitude and uses acceleration to offset gravity; Liquid buoyancy balance gravity method, so that the test piece is immersed in water; Non-contact suspension method, which includes a variety of electromagnetic suspension, air suspension, acoustic suspension, electrostatic suspension, light suspension, particle suspension and so on. The hanging wire system is a test system that connects the experimental target and the gravity compensation device through the pulley block and the hanging wire to simulate the ground micro-gravity environment. Compared with other systems, this system is simple in structure and easy to implement. The experiment time can be adjusted freely to ensure sufficient and reliable data.

In order to verify the correctness of the theoretical repeat positioning accuracy, this article uses the following verification method. The coordinate system is established with the center of the interface *A* as the origin of coordinates, and the directions of the *XYZ* three coordinate axes are shown in Fig. 8. The models of the two autocollimators are Collapex AC300, the measurement accuracy is 0.015''. The layout of the autocollimator is shown in 2 and 3 in Fig. 8, 2 and 3 are matched with plane mirrors 4 and 5 on the module respectively. Autocollimator 2 measures the rotation angle of the module in the *Y* and *Z* directions, and autocollimator 3 measures the rotation angle of the module in the *X* direction. The model of laser tracker 1 is Leica AT960, the measurement accuracy is 2μm. The laser tracker measures the four target balls (6789) which on the same plane of the module, and calculates the six degrees of freedom of the module according to the coordinate changes of these four points measured by the laser tracker. At the same time, it is compared with the measurement results of the autocollimator to verify the measurement angle of the autocollimator.
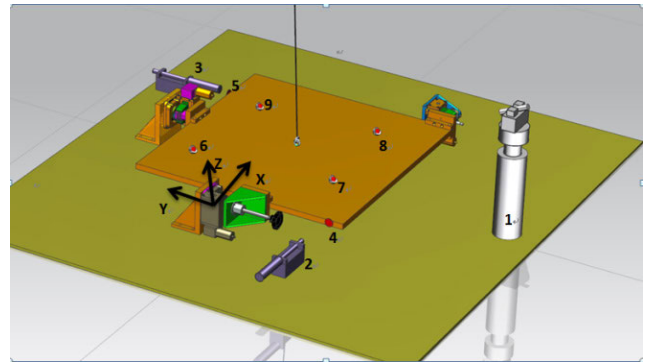

FIGURE 8. Experimental schematic diagram.

In order to obtain the repeated positioning accuracy of the measured objects, the least square method is used to fit the data measured by the laser tracker. The data processing of the laser tracker is as follows: Definition

$$E = \sum_i ((d_{Xi} - d'_{Xi})^2 + (d_{Yi} - d'_{Yi})^2 + (d_{Zi} - d'_{Zi})^2) \quad (30)$$

Equation (30) is our objective function, where d'_i is the point displacement data measured by the laser tracker, and d_i is the real point displacement of the module. So substitute (27) into (30) and solve for it.

$$E = \sum_i [(d_{Xi} + Y_i R_Z - Z_i R_Y - T_X)^2 + (d_{Yi} - X_i R_Z + Z_i R_X - T_Y)^2 + (d_{zi} + X_i R_Y - Y_i R_X - T_Z)^2] \quad (31)$$

Find the partial derivatives of the rotation angle of objective function *E* and the partial derivatives of the translation of objective function *E* in turn, and make the partial derivatives equal to zero. We can get the system of linear equations with

six variables. By solving the equations, we can get the rotation angle and translation of the rigid body.

$$
\begin{cases}
\dfrac{\partial E}{\partial T_X} = \sum_i (-Y_i R_Z + Z_i R_Y + T_X - d_{xi}) = 0 \\[2mm]
\dfrac{\partial E}{\partial T_Y} = \sum_i (X_i R_Z - Z_i R_X + T_Y - d_{yi}) = 0 \\[2mm]
\dfrac{\partial E}{\partial T_Z} = \sum_i (-X_i R_Y + Y_i R_X + T_Z - d_{zi}) = 0 \\[2mm]
\dfrac{\partial E}{\partial R_X} = \sum_i (Y_i(-X_i R_Y + Y_i R_X + T_Z) - Z_i(X_i R_Z \\[2mm]
\qquad -Z_i R_X + T_Y) - Y_i d_{zi} + Z_i d_{yi}) = 0 \\[2mm]
\dfrac{\partial E}{\partial R_Y} = \sum_i (Z_i(-Y_i R_Z + Z_i R_Y + T_X) \\[2mm]
\qquad -X_i(-X_i R_Y + Y_i R_X + T_Z) - Z_i d_{xi} + X_i d_{zi}) = 0 \\[2mm]
\dfrac{\partial E}{\partial R_Z} = \sum_i (X_i(X_i R_Z - Z_i R_X + T_Y) \\[2mm]
\qquad -Y_i(-Y_i R_Z + Z_i R_Y + T_X) - X_i d_{yi} + Y_i d_{xi}) = 0
\end{cases}
\tag{32}
$$

Before the experiment, the coordinate system of the laser tracker is transformed. The global coordinate system of the laser tracker is converted according to the coordinates of known points on the workpiece, and the coordinates of the target ball to be measured by the back-end module are compensated at the same time. The compensation consists of two parts: In the *Z* direction, one part is the radius of the target ball and the other part is half of the thickness of the experimental piece, and the *XY* direction is only the radius of the target ball. Verify the facula stability of the two instruments in a laboratory environment. The laser tracker continuously records the spatial coordinates of four target balls for 30 minutes, and calculates the spatial coordinate changes of the four target balls. The maximum standard deviations of the coordinate changes of the four target balls in the *XYZ* directions are 0.38μm, 0.43μm and 0.40μm. The two autocollimations were also continuously record for 30 minutes, and the rotation angular standard deviations of the module in the *XYZ* directions were calculated as 0.0051'', 0.0063'' and 0.0054''. The test results show that the facula of the two measuring instruments have high stability within 30 minutes, meeting the requirements of the precision measurement of the system, and the effect of facula drift is negligible. This experiment uses a hanging wire system to unload the gravity of the module. The hanging wire system includes fixed pulley, hanging wire, hanging frame, and counterweight. The fixed pulley is installed on the hanging frame, the hanging wire passes through the fixed pulley, one end is connected the module, and the other end is connected the counterweight with the same weight as the module. By adjusting the mass of the counterweight, the whole experimental device can finally realize microgravity simulation of the order of magnitude 0.001g. On-orbit maintenance feasibility test and repeated positioning measurement device are shown in Fig. 9.

TABLE 2. Experimental Results Measured by Laser Tracker.

|	The laser tracker measures the coordinates of the target ball					
	X1	Y1	Z1	X2	Y2	Z2
1	98.725	175.231	0.001	99.04	-180.457	0.002
2	98.724	175.236	-0.006	99.051	-180.452	0.007
3	98.726	175.231	-0.004	99.05	-180.457	0.001
4	98.726	175.232	0.002	99.04	-180.456	-0.001
5	98.729	175.224	-0.007	99.034	-180.464	0.006
6	98.729	175.234	0.005	99.045	-180.453	0.005
7	98.718	175.233	0.002	99.044	-180.454	-0.008
8	98.721	175.227	0.005	99.036	-180.46	0.001
9	98.733	175.228	-0.003	99.035	-180.459	0.01
10	98.729	175.225	0.002	99.045	-180.462	0.008
11	98.729	175.227	0.007	99.036	-180.46	0.001
	X3	Y3	Z3	X4	Y4	Z4
1	248.023	-179.017	0.001	248.806	176.451	0
2	248.034	-179.007	0.008	248.806	176.461	-0.004
3	248.033	-179.014	0.005	248.809	176.454	0.002
4	248.022	-179.018	-0.005	248.809	176.45	0
5	248.016	-179.03	0.007	248.812	176.438	-0.004
6	248.027	-179.015	0.008	248.812	176.453	0.011
7	248.026	-179.012	-0.012	248.801	176.456	0.001
8	248.018	-179.023	0.003	248.803	176.445	0.01
9	248.017	-179.027	0.007	248.815	176.441	-0.004
10	248.027	-179.024	0.001	248.811	176.444	-0.003
11	248.018	-179.025	0.001	248.811	176.443	0.009
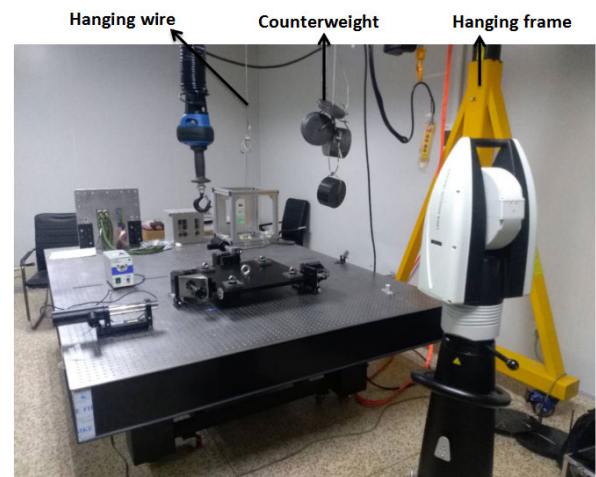
FIGURE 9. Field experiment diagram.

B. ANALYSIS OF EXPERIMENTAL DATA

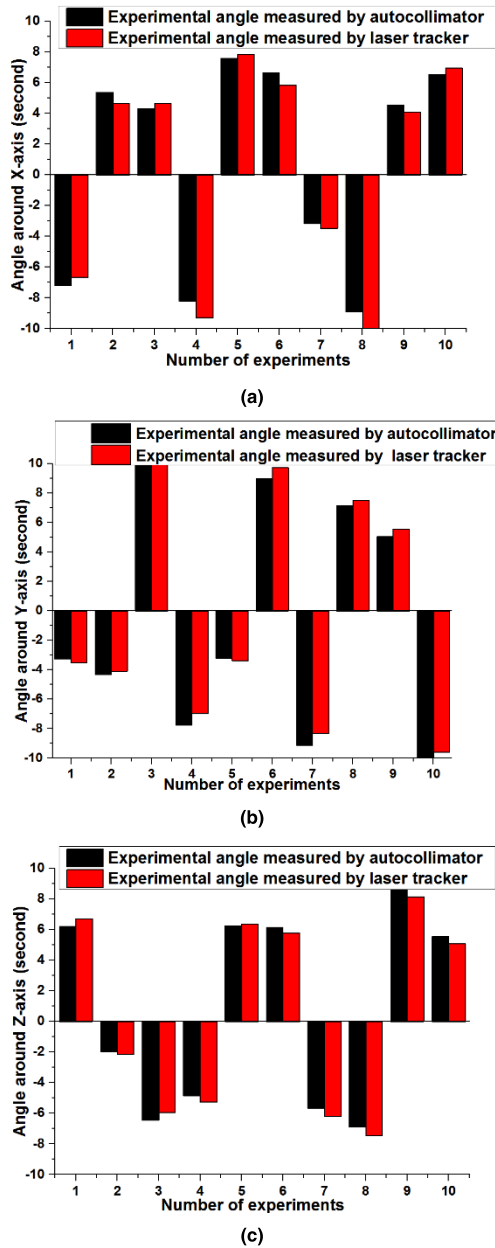Table 2 is the record result of 10 times plugging and unplugging the module measured by the autocollimator, and

FIGURE 10. The rotation angles of the module in *XYZ* directions measured by two kinds of instruments. (a) Rotation angle around X-axis; (b) Rotation angle around Y-axis; (c) Rotation angle around Z-axis.

Table 3 is the record result of the four target balls measured by the laser tracker. Process the data recorded by the tracker according to (32). As shown in Fig. 9: The rotation angles of the module in *XYZ* directions measured by two kinds of instruments.

According to the Grubbs criterion, there is no gross error in the measured data. Based on the analysis of the experimental data, the rotation angle measured by the autocollimator is taken as the reference. The maximum error of the angle measured by the laser tracker relative to the data of the autocollimator in the three directions of *XYZ* is less than 11% (as shown in Fig. 11), which proves that the rotation angle measured by the two instruments is true and reliable.

TABLE 3. Experimental Results Measured by Autocollimator.

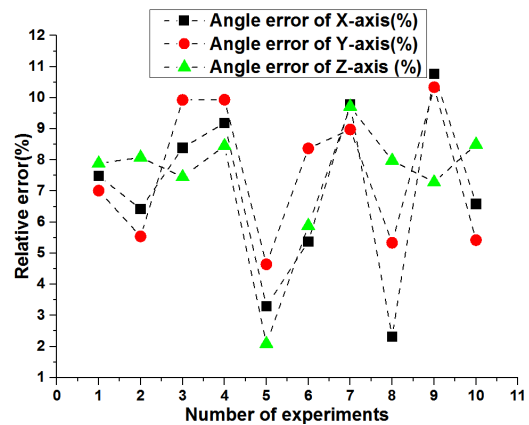|	Autocollimator record value		
	angle around the X-axis(″)	angle around the Y-axis(″)	angle around the Z-axis(″)
1	14.28	42.36	-56.34
2	7.07	39.08	-50.13
3	11.43	34.75	-52.11
4	15.72	44.82	-58.55
5	5.49	37.87	-63.4
6	13.07	34.64	-57.17
7	19.21	43.6	-51.05
8	16.04	34.47	-56.71
9	6.12	41.59	-63.6
10	10.67	46.62	-54.82
11	17.19	36.48	-49.69

FIGURE 11. The error of rotation angle measured by laser tracker relative to autocollimator.

The repeated positioning accuracy of the module measured by the experiment is (33) [21].

$$\sigma = 3S \tag{33}$$

where the standard deviation *S* is (34)

$$S = \sqrt{\frac{\sum\limits_{i=1}^{n} (x_i)^2}{n-1}} \tag{34}$$

In the (34), X_i is the residual of displacement or rotation angle, and *n* is the number of measurements. Calculation (33)-(34): It can be seen that the repeat positioning accuracy of the rotation angle in the *XYZ* directions measured by the autocollimator is $\pm13.9''$, $\pm13.3''$ and $\pm14.7''$; The repeat positioning accuracy of the rotation angle in the *XYZ* directions measured by the laser tracker is $\pm14.3''$, $\pm14.4''$ and $\pm14.6''$ (as shown in Fig. 12-a). Both measurement results are better than the index. The repeat positioning accuracy of translation in the *XYZ* directions measured by the laser tracker is $\pm9.3\mu m$, $\pm9\mu m$ and $\pm10\mu m$ (as shown in Fig. 12-b).
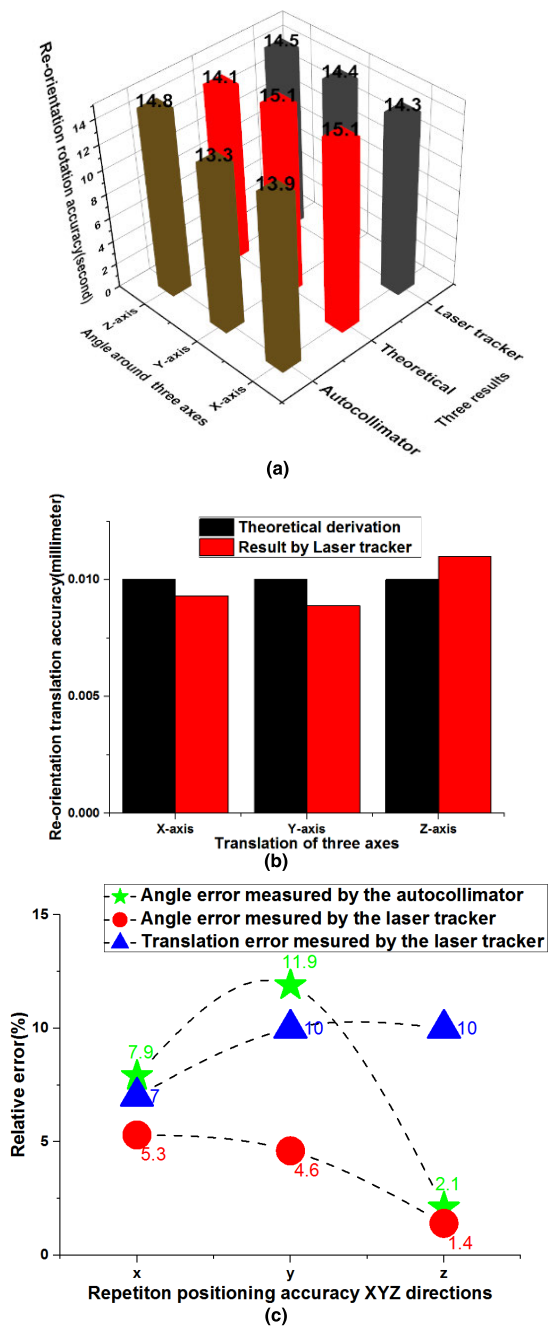
(a)

(b)

(c)

FIGURE 12. **Experimental and theoretical repeat positioning accuracy.**
(a) rotation angle repeat positioning accuracy in *XYZ* directions;
(b) Translation repeat positioning accuracy in *XYZ* directions; (c) The error
of the module repeat positioning accuracy measured by the two
instruments relative to the theoretical repeat positioning accuracy.

During the experiment of the two instruments, the measured repeat positioning accuracy are slightly lower than the theoretical value in the *XY* directions, and slightly higher than the theoretical value in the *Z* direction. Analyzing the experimental data and taking the theoretical repeat positioning accuracy as the benchmark, it can be seen that the max error of the module repeat positioning accuracy measured by the two instruments relative to the theoretical repeat positioning accuracy is less than 12% (as shown in Fig. 12-c). However,

there are some acceptable errors between experimental results and theoretical derivation due to errors in machining, installation, and personnel etc. Which is basically consistent with the theoretical results, to prove that the experimental data is true and reliable.

VI. CONCLUSION

In this article, taking the on-orbit maintenance of the space telescope as the research object, referring to the kinematics principle, a detailed design of a set of interface mechanisms that can meet its on-orbit rapid disassembly and installation. The repeated positioning accuracy of the module is calculated according to the homogeneous coordinate transformation, a simplified change matrix is obtained. The relationship between the theoretical rotation angle and the fitting clearance is derived, and the fitting clearance of the mechanism is designed with the rotation angle index as a constraint. A method combining autocollimator and laser tracker is proposed to measure the repeat positioning accuracy of the module. The error between the angle repetition positioning accuracy of the module in *XYZ* directions measured by the autocollimator and theoretical value is 7.9%, 11.9%, 2.1%. The error between the angle repetition positioning accuracy of the module in *XYZ* directions measured by the laser tracker and theoretical value is 5.3%, 4.6%, 1.4%. The error between the translation repetition positioning accuracy of the module in *XYZ* directions measured by the laser tracker and theoretical value is 7%, 10%, 10%. The experimental results are basically consistent with the theoretical results, that is, the correctness of the theoretical results is verified. It is also verified that the laser tracker can measure the six degrees of freedom of a rigid body when the accuracy is allowed. It provides reference for other on-orbit repairable interface system.

REFERENCES

[1] K. Dan, "Hubble robotic servicing: Stepping stone for future exploration missions," in *Proc. 1st Space Explor. Conf., Continuing Voyage Discovery*, 2005, p. 2524.

[2] N. GSFC, "On-orbit satellite Servicing study project report," NASA, Greenbelt, MD, USA, Project Report NP-2010-08-162-GSFC, 2010.

[3] B. R. Mccullar, "Solar maximum repair mission," in *Nat. Symp. Workshop Opt. Platforms Int. Soc. Opt. Photon.*, vol. 493, 1984, pp. 73–78.

[4] D. C. Alhorn, "Autonomous assembly of modular structures in space and on extraterrestrial locations," in *AIP Conf. Amer. Inst. Phys.*, vol. 746, 2005, pp. 1121–1128.

[5] M. Oda, K. Kibe, and F. Yamagata, "ETS-VII, space robot in-orbit experiment satellite," in *Proc. IEEE Int. Conf. Robot. Autom.*, Apr. 1996, pp. 739–744.

[6] S. Shane, "Orbital express capture system: Concept to reality," *Proc. SPIE*, vol. 5419, pp. 78–91, Aug. 2004.

[7] A. Flores-Abad, O. Ma, K. Pham, and S. Ulrich, "A review of space robotics technologies for on-orbit servicing," *Prog. Aerosp. Sci.*, vol. 68, no. 8, pp. 1–26, Jul. 2014.

[8] Daukantas *et al.*, "Hubble's final servicing mission," *Opt. Photon. News*, vol. 19, no. 10, pp. 30–35, 2008.

[9] S. Thomas *et al.*, "Hubble space telescope first servicing mission and observatory recommissioning," in *Proc. Space Astronomical Telescopes Instrum. II, Int. Soc. Opt. Photon.*, vol. 1945, 1993, pp. 11–16.

[10] P. Hansen, "Hubble Space Telescope second servicing mission contamination control program," *Proc. SPIE*, vol. 2864, pp. 27–35, Nov. 1996.

[11] R. Kimble, "Wide field camera 3: A powerful new imager for the Hubble space telescope," *Proc. SPIE*, vol. 7010, Jul. 2008, Art. no. 70101E.

[12] D. King, "Hubble robotic servicing: Stepping stone for future exploration missions," in *Proc. 1st Space Explor. Conference: Continuing Voyage Discovery*, Jan. 2005, p. 2524.

[13] X. Chen, C. Fang, X. Li, B. Zhan, and Q. He, "A new temperature compensation method for microbolometric focal plane array," *Optik*, vol. 127, no. 18, pp. 7132–7136, Sep. 2016.

[14] Y. A. Zhang, C. F. Lin, J. P. Lin, X. Y. Zeng, Q. Yan, X. T. Zhou, and T. L. Guo, "Dual-layer electrode-driven liquid crystal lens with electrically tunable focal length and focal plane," *Opt. Commun.*, vol. 412, pp. 114–120, Apr. 2018.

[15] J. Li and Z. Liu, "Optical focal plane based on MEMS light lead-in for geometric camera calibration," *Microsyst. Nanoeng.*, vol. 3, no. 1, p. 17058, Dec. 2017.

[16] R. Arora and B. S. Rajpurohit, "An experimental investigation of electrical clearance in air for overhead traction system," *IEEE Access*, vol. 8, pp. 105766–105774, 2020.

[17] M. Xu, G. Feng, Q. He, F. Gu, and A. Ball, "Vibration characteristics of rolling element bearings with different radial clearances for condition monitoring of wind turbine," *Appl. Sci.*, vol. 10, no. 14, p. 4731, Jul. 2020.

[18] Y. K. Gu, W. F. Li, J. Zhang, and G. Q. Qiu, "Effects of wear, backlash, and bearing clearance on dynamic characteristics of a spur gear system," *IEEE Access*, vol. 7, pp. 117639–117651, 2019.

[19] F. Teng, X. Zhang, and S. Xie, "Research on variation mechanism of three-dimensional blade tip clearance of aero-engine," in *Proc. 13th Int. Conf. Ubiquitous Robots Ambient Intell. (URAI)*, Aug. 2016, pp. 1–6.

[20] W. Wang, "Current status and developing tendency of visible spectral remote sensing camera for mars observation," *Chin. Opt.*, vol. 7, no. 2, pp. 208–214, 2014.

[21] Y. T. Fei, *Error Theory and Data Processing*. Hefei, China: Hefei Univ. Technology, 2014, pp. 12–24.

ZHEN SHI was born in Dezhou, Shandong, China, in 1992. He received the B.S. degree in mechanical design manufacture and automation from Liaocheng University, China, in 2015. He is currently pursuing the Ph.D. degree in mechanical design manufacture and automation with the Changchun Institute of Optics, Fine Mechanics and Physics, Chinese Academy of Sciences, Changchun, China. He is current research interest includes the application of on-orbit maintenance.

WEIGUO ZHAO was born in Daqing, Heilongjiang, China, in 1985. He received the B.S. degree in mechanical design manufacture and automation and the M.S. degree in mechanical design manufacture and automation from Xi'an Jiaotong University, China, in 2008 and 2010, respectively. Since 2010, he has been the Group Leader of the Space Optics Laboratory, Changchun Institute of Optics, Fine Mechanics and Physics, Chinese Academy of Sciences. His current research interests include design and research on optical mechanical structure and the spatial mechanism of space optical remote sensor.

LIBAO YANG was born in Tangshan, Hebei, China, in 1972. He received the B.S. degree in optics, fine mechanics and physics and the Ph.D. degree from the Changchun University of Science and Technology, China, in 1995 and 2017, respectively. Since 2004, he has been with the Space Optics Laboratory, Changchun Institute of Optics, Fine Mechanics and Physics, Chinese Academy of Sciences. His research interests include research on the overall design of optical instruments and the on-orbit maintenance technology of space optical payload.

YANG XUN was born in Changchun, Jilin, China, in 1986. He received the B.S. and M.S. degrees in mechanical design manufacture and automation from Jilin University, China, in 2008 and 2010, respectively, and the Ph.D. degree from Shanghai Jiao Tong University, Shanghai, China, in 2016. Since 2016, he has been with the Finite Element Simulation Laboratory, Changchun Institute of Optics, Fine Mechanics and Physics, Chinese Academy of Sciences. His current research interests include design and research on optical mechanical structure and the finite element simulation of space optical remote sensor.

QINGYA LI was born in Daqing, Heilongjiang, China, in 1993. She received the B.S. degree in mechanical design manufacture and automation from Northeast Agricultural University, China, in 2015. She is currently pursuing the Ph.D. degree in mechanical design manufacture and automation with the Changchun Institute of Optics, Fine Mechanics and Physics, Chinese Academy of Sciences, Changchun, China. Her current research interests include the application of on-orbit maintenance and spacecraft structure design.

YAOYU ZHANG was born in Siping, Jilin, China, in 1973. He received the B.S. degree in mechanical design manufacture and automation from Jinlin University, China, in 2008, and the Ph.D. degree in mechanical design manufacture and automation from the Changchun Institute of Optics, Fine Mechanics and Physics, Chinese Academy of Sciences, Changchun, China, in 2003. Since 2005, he has been the Director of the Measurement and Control Laboratory, Changchun Institute of Optics, Fine Mechanics and Physics, Chinese Academy of Sciences. His current research interests include e-precision tracking measurement technology, deformation measurement, and theodolite structure design.

• • •